




Turbulent characteristics and energy transfer in the far field of active-grid turbulence

Cite as: Phys. Fluids **33**, 115119 (2021); <https://doi.org/10.1063/5.0070912>

Submitted: 10 September 2021 • Accepted: 07 October 2021 • Published Online: 16 November 2021

 Y. Zheng (鄭玉霖),  K. Nagata (長田孝二) and  T. Watanabe (渡邊智昭)



View Online



Export Citation



CrossMark

ARTICLES YOU MAY BE INTERESTED IN

Energy dissipation and enstrophy production/destruction at very low Reynolds numbers in the final stage of the transition period of decay in grid turbulence

Physics of Fluids **33**, 035147 (2021); <https://doi.org/10.1063/5.0041929>

Meandering of a wing-tip vortex in a grid-generated turbulent flow

Physics of Fluids **33**, 115131 (2021); <https://doi.org/10.1063/5.0057083>

Detailed investigation of subgrid scale models in large-eddy simulation using high aspect-ratio grid spacing

Physics of Fluids **33**, 115120 (2021); <https://doi.org/10.1063/5.0070183>

APL Machine Learning

Open, quality research for the networking communities

OPEN FOR SUBMISSIONS MAY 2022

LEARN MORE

Turbulent characteristics and energy transfer in the far field of active-grid turbulence

Cite as: Phys. Fluids **33**, 115119 (2021); doi: [10.1063/5.0070912](https://doi.org/10.1063/5.0070912)

Submitted: 10 September 2021 · Accepted: 7 October 2021 ·

Published Online: 16 November 2021



View Online



Export Citation



CrossMark

Y. Zheng (鄭玉霖), K. Nagata (長田孝二), ^{a)} and T. Watanabe (渡邊智昭)

AFFILIATIONS

Department of Aerospace Engineering, Nagoya University, Nagoya, Japan

^{a)} Author to whom correspondence should be addressed: nagata@nagoya-u.jp

ABSTRACT

Turbulent characteristics in the far field of active-grid turbulence have been investigated through wind tunnel experiments using hot-wire anemometry. Two forcing protocols are employed following previous studies: one is the double-random mode and the other is the open mode with the grid remaining static with minimum blockage. The integral length scale L for the double-random modes slightly decreases with streamwise distance in the far field as observed in the near field of the active-grid turbulence. The nondimensional dissipation rate C_ϵ for the double-random modes is around 0.5. This asymptotic value is different from those reported in previous active-grid turbulence experiments and could be nonuniversal. The equilibrium scaling $L/\lambda = C_\epsilon Re_\lambda/15$ (λ is the Taylor microscale and Re_λ is the turbulent Reynolds number) with a constant C_ϵ is established in the far field of the double-random modes regardless of active-grid motions. The sum of production and destruction terms in the enstrophy budget equation for homogeneous and isotropic turbulence $S + 2G/Re_\lambda$ (S is the skewness of the longitudinal velocity derivative and G is the destruction coefficient) is proportional to Re_λ^{-1} and close to zero in the present active-grid turbulence, suggesting that the equilibrium scaling is possibly related to the balance between the production and destruction of the enstrophy.

Published under an exclusive license by AIP Publishing. <https://doi.org/10.1063/5.0070912>

I. INTRODUCTION

Turbulence is an abstruse phenomenon, playing critical roles in industrial flows, atmospheric flows, and so on. Homogeneous isotropic turbulence (HIT) simplifies the problems related to turbulence by assuming statistical homogeneity and isotropy, and it has been extensively investigated by theories, direct numerical simulations (DNSs), and wind tunnel experiments of grid turbulence.^{1–6} One of the most underlying theories of turbulent flows is proposed by Kolmogorov^{2,7} on the premise of an infinite turbulent Reynolds number $Re_\lambda = u_{\text{rms}}\lambda/\nu$ [where u_{rms} is the root mean square (rms) of velocity fluctuations u , λ is the Taylor microscale, and ν is the kinematic viscosity]. However, grid turbulence generated in laboratories and DNSs has been suffering from low- Re_λ limitation. Since the first active-grid-design introduced by Makita,⁸ the active grid has been commonly used to generate quasi-HIT in a wind tunnel with a high Re_λ level. In contrast to passive grids with stationary horizontal and vertical bars, the active grid consisting of rotating bars with winglets is capable of generating higher Re_λ turbulence in a laboratory-sized wind tunnel.^{8–11} Therefore, the active grid is extensively utilized in experimental studies on unsteady turbulence,¹² further understanding of the theoretical hypotheses governed by turbulence with sufficiently high Re_λ ,^{13,14} and investigating the turbulent production mechanism.¹⁵

Makita⁸ measured a turbulent kinetic energy (TKE) of the active grid up to the streamwise distance $x/M \approx 100$ with a mesh size $M = 46.7$ mm and $Re_\lambda \approx 400$ using the single-random mode (i.e., the rotation rate is fixed and the rotation period changes randomly). The power-law exponent of TKE $n = 1.43$ is achieved with an acceptable homogeneous and isotropic state. Later, Mydlarski and Warhaft⁹ followed the design of Makita and made detailed analyses of turbulent characteristics using the single-random mode with $Re_\lambda \approx 500$, where $n = 1.21$ is obtained up to $x/M \approx 70$. Since then, many researchers have been focusing on how the characteristics of grid turbulence depend on the way by which the turbulence is generated. For instance, Larssen and Devenport¹⁰ developed an active grid with a 2.14 m square, whose Re_λ is up to 1360 using the double-random mode (i.e., both the rotation rate and period change randomly). They concluded that the grid Reynolds number $Re_M (= MU/\nu$, where U is the mean velocity) and the Rossby number $Ro (= U/\Omega M$, where Ω is the mean rotation rate) are the two most significant controlling parameters for the turbulent characteristics of active-grid turbulence. Hearst and Lavoie¹⁵ later ascertained variations of the produced active-grid turbulence with different controlling parameters.

Meanwhile, other types of grids such as fractal grids are also utilized to generate quasi-HIT with high Re_λ , and its flow characteristics

have been investigated extensively. For instance, Valente and Vassilicos¹⁶ assessed the fractal-grid turbulence up to $x/M \approx 18$ with the highest Re_λ of 350. They found that the fractal-grid turbulence broke the equilibrium scaling ($\varepsilon = C_\varepsilon u_{\text{rms}}^3/L$ and $L/\lambda = C_\varepsilon Re_\lambda/15$) with a constant C_ε , where ε is the dissipation rate of TKE, C_ε is the nondimensional dissipation rate, and L is the integral length scale. Furthermore, Valente and Vassilicos¹⁷ proved that the nonequilibrium scaling was also manifested in the near field of conventional passive-grid turbulence, as also confirmed later by Isaza *et al.*¹⁸ and Hearst and Lavoie.¹⁹ To the end, whether the assessed decay region is near, or far field is a key point of illustrating flow properties of grid turbulence. However, compared with well-investigated turbulence generated by passive grids (e.g., conventional and fractal grids), further investigations of turbulent characteristics have not been given in the far field of active-grid turbulence. Moreover, dense measuring points within the far downstream region are necessary for investigating the decay characteristics of TKE in active-grid turbulence. Thormann and Meneveau²⁰ investigated the power-law decay exponent n of TKE for the double-random mode of active-grid and active-fractal-grid turbulence. The decay exponent n obtained in their active-grid turbulence is in the range 1.0–1.3 for $15 < x/M < 50$. They also obtained $C_\varepsilon \approx 1$ and observed that C_ε evolves slowly in the downstream direction in the active-grid turbulence. Mora *et al.*¹³ examined energy cascades of active-grid turbulence in the near field (x/M up to nearly 30). It was identified that although L decreased with the streamwise distance, the active-grid turbulence followed the equilibrium scaling in the near field. However, smaller C_ε close to 0.3 was obtained in their active-grid turbulence. Also, Gamard and George²¹ reanalyzed the experimental data of Mydlarski and Warhaft⁹ measured at $x/M = 68$ and computed that C_ε ranges from 0.7 to 1.1. Generally, unlike passive-grid turbulence, a wide range of n and C_ε has been reported in previous studies. The dominant factors that determine them are not clear at all because of lacking experimental data on active-grid turbulence, especially in the far field. Whether the flow properties will vary only with Re_λ or they also depend on the initial conditions still needs further investigations.

In addition, the balance between production and destruction of enstrophy has been investigated in passive-grid turbulence.^{6,22–24} The production and destruction of enstrophy in HIT are, respectively, represented by $-S$ and $2G/Re_\lambda$. Here,

$$S = \overline{\left(\frac{\partial u}{\partial x}\right)^3} / \left[\overline{\left(\frac{\partial u}{\partial x}\right)^2} \right]^{\frac{3}{2}}, \quad G = u_{\text{rms}}^2 \overline{\left(\frac{\partial^2 u}{\partial x^2}\right)^2} / \left[\overline{\left(\frac{\partial u}{\partial x}\right)^2} \right]^2 \quad (1)$$

are the derivative skewness and the destruction coefficient, respectively.²⁵ The overline $\bar{*}$ denotes an ensemble average of $*$. Thiesset *et al.*²⁴ showed at infinite Reynolds number $S + 2G/Re_\lambda \propto Re_\lambda^{-1}$ along the centerline of an axisymmetric jet and in purely decaying turbulence, although its functional form is different due to different large-scale forcing. Therefore, they noticed that the dependence of $S + 2G/Re_\lambda$ on Re_λ may differ from flow to flow and should be investigated separately in each flow.²⁴ However, the experimental assessment of $S + 2G/Re_\lambda$ in active-grid turbulence has not been given so far. It is interesting to investigate whether or not the dependence of $S + 2G/Re_\lambda$ on Re_λ in active-grid turbulence is similar to that in

passive-grid turbulence since the active-grid turbulence could have different large-scale properties.

The objective of the present study is to investigate turbulent characteristics in the far field of active-grid turbulence. Measurements of C_ε of the active-grid turbulence are conducted to figure out the far-field behavior of C_ε . The equilibrium scaling of the active-grid turbulence is also examined. The present study also assesses the production and destruction terms in the enstrophy budget equation and offers updated profiles for the Re_λ dependence in the far field of active-grid turbulence.

This paper is organized as follows: In Sec. II, we briefly describe the wind tunnel, active-grid setup, and measurements. Section III presents the experimental results for the streamwise variations of turbulent characteristics up to the far field and the statistics related to the energy cascade and the enstrophy evolution. Finally, Sec. IV summarizes conclusions.

II. EXPERIMENTAL SETUP

A. Wind tunnel and active grid

The experiments are performed in an open-type wind tunnel at Nagoya University, the same as used in Zheng *et al.*⁶ The test section has a $0.6 \times 0.6 \text{ m}^2$ cross section, and its length is 12 m. The contraction ratio of the wind tunnel is 9 : 1. The active grid (see Fig. 1) is installed at the entrance to the test section. The coordinate system is expressed in x , y , and z coordinates, which describe the streamwise, vertical, and lateral directions, respectively. The origin is located at the center of the grid.

The active-grid design follows the original design of Makita,⁸ Mydlarski and Warhaft,⁹ and Larssen and Devenport.¹⁰ The mesh size $M = 75 \text{ mm}$ is chosen to satisfy the homogeneity and to generate high Re_λ , resulting in $8M \times 8M$ arrangement of the horizontal and vertical rotating axes mounted with winglets.^{9,26} The solid winglets are made of polylactic acid (PLA) resin and manufactured by using a 3D printer. They have a diamond shape and arranged in biplane. The thickness and diagonal of each winglet are 2 and 60 mm, respectively. The diagonal of each winglet is smaller than M to avoid collisions of adjacent winglets during rotations. The rotating axes are made of hollow steel cylinders to reduce the inertial moments. The diameter of the rotating axes is 10 mm. The rods are fastened to the coupling through a ball bearing to suppress the vibration by rotation, and the coupling and stepping motor are connected through an aluminum wall. The horizontal and vertical rods have 3 mm gaps, connected by some joints to reduce vibrations.

The rotation of each rod is individually performed by a stepping motor (Oriental Motor, PKP268D28A2), driven by a motor driver (Oriental Motor, CVD228BR-K). Four AC–DC converters (TDK, HWS100A-24/A) and two motor controllers (Y2, PMC-S8/00/00A-U) are used as a power supply and signal-controlling, respectively. The forcing protocols of the active grid are programed in a personal computer. In the present study, the double-random mode and the open mode are chosen as the forcing protocols. The double-random mode is widely used in previous studies of active-grid turbulence, since it can generate turbulence with a good HIT condition and high Re_λ and does not yield spikes in an energy spectrum at low wavenumber regions.^{10,11,13} For the double-random mode, all motors are driven randomly with rotation rates varying in a fixed range, and directions of rotating are switched randomly in time. The mean rotation rate Ω ,

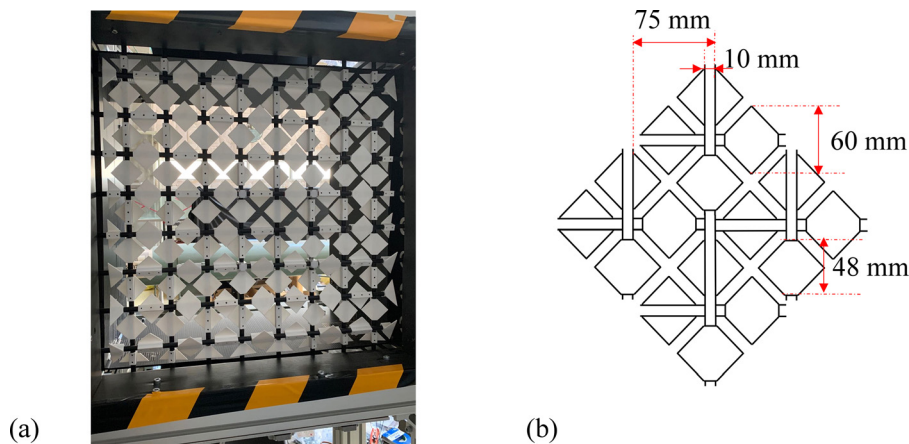


FIG. 1. (a) Picture of the active grid used in the present study. (b) Schematic of the grid with the maximum blockage.

the maximum deviation of the rotation rate ω , the mean time interval until the reversal T , the maximum deviation of the time interval t , and the Rossby number R_o are shown in Table I. In contrast, the grid remains static with the minimum blockage for the open mode, which is similar to passive grids used in previous studies.⁶ The grid Reynolds number Re_M is 33 000 for all the cases.

B. Measurements

Instantaneous streamwise velocity is measured using constant-temperature hot-wire anemometry (Dantec Dynamics, Streamline) with an I-type probe (Dantec Dynamics, 55P01 and 55P11). The probe 55P11 is a conventional I-type probe and is used in case 3. Since the double-random mode of the active grid is capable of generating higher turbulent levels, 55P01 probe is used for measurements of cases 1 and 2. The wire ends of this probe are copper- and gold-plated, leaving an active sensor on the middle of the wire. The construction of this probe is designed for measurements in high-turbulence flows. The sensor length of both probes is 1.25 mm, and their diameter is $5\ \mu\text{m}$, so that the aspect ratio is 250. The overheat ratio is set to 0.8. The sampling number and frequency are set to 8 388 608 and 50 kHz, respectively, aiming to acquire reliable statistics. The signal is amplified by a signal conditioner and then recorded and sent to a personal computer from an A/D converter (National Instruments, NI-9215). A standard pitot tube is used to calibrate the hot-wire probe in the wind tunnel with a small background turbulent intensity. We used the fourth-order polynomial fit in the calibration of the hot-wire anemometry. The eighth-order Butterworth low-pass filter is applied for the time series of data to remove the high-frequency noise inevitably contained in the signal. The cutoff frequency is set at the Kolmogorov frequency $f_k = U/2\pi\eta$, where $\eta = (\nu^3/\epsilon)^{1/4}$ is the Kolmogorov scale. This filtering technique is the same as used in Mi *et al.*²⁷ and Hearst and Lavoie.¹⁵

The homogeneity of active-grid turbulence has been assessed in several previous studies.^{8–10,26} It has been demonstrated that the active-grid turbulence operated in the random mode is statistically homogeneous if the wind tunnel width is roughly ten times larger than the mesh size.²⁶ In the present study, the measurement points locate along the streamwise direction at the center of the wind tunnel cross section, and M equals to 12.5% of the wind tunnel width. Therefore, we consider that the measurements are conducted in a quasi-homogeneous region of the active-grid turbulence. Mora *et al.*¹³ showed that the active-grid turbulence exhibits acceptable isotropy in the double-random mode for $x/M > 10$. Hearst and Lavoie¹⁵ tested different control parameters of the active grid and found that the isotropy increases with decreasing R_o . Larssen and Devenport¹⁰ showed that the anisotropy ratio, defined as the ratio between the longitudinal and transverse rms velocity fluctuations, is in the range 1.1–1.2 for $R_o < 50$ and is around 1.2 for $50 < R_o < 100$. Moreover, Shet *et al.*¹¹ proposed that higher isotropy of active-grid turbulence attributes to higher tip speed ratio $\alpha = 2C_w\pi\Omega/U$ ($2C_w$ is the diagonal of the winglet), and their flow becomes approximately isotropic at $\alpha = 0.08$. In the present study, main measurements are performed within the far-downstream region ($x/M > 50$), and the operating protocol is the same as used in Mora *et al.*¹³ The values of R_o are in the acceptable range for attaining isotropy confirmed by Larssen and Devenport¹⁰ (i.e., $R_o < 100$). The values of α of cases 1 and 2 are 0.06 and 0.03, respectively, and satisfy the condition for high isotropy obtained by Shet *et al.*¹¹

III. RESULTS AND DISCUSSION

A. Decay of turbulent intensity

Figure 2 shows the decay of turbulent intensity for the double-random and open modes. Compared with the open mode, the double-

TABLE I. Control parameters of the active grid.

Case	Mode	$\Omega \pm \omega$ (Hz)	$T \pm t$ (s)	Solidity	R_o	M (mm)	Re_M
1	Double random	2 ± 0.2	2 ± 1	0.39 – 0.69	40	75	33 000
2	Double random	1 ± 0.2	2 ± 1	0.39 – 0.69	80	75	33 000
3	Open	0.39	...	75	33 000

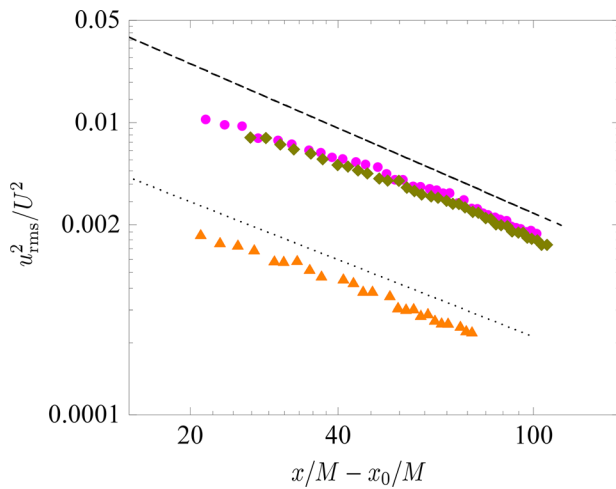


FIG. 2. Decay of turbulent intensity with streamwise distance from a virtual origin x_0 . The dashed and dotted lines represent the slopes $n=1.46$ and $n=1.32$, respectively. For symbols, see Table II.

random modes produce much higher levels of turbulent intensity.⁸ For the double-random mode with the same Re_M , turbulent intensity is slightly larger for higher Re_σ , which is consistent with previous studies.^{11,15} In wind tunnel experiments of grid turbulence, the following power-law decay form is broadly accepted for investigating the decay of TKE,^{4–6,8,9,11,28}

$$\frac{u_{rms}^2}{U^2} = a \left(\frac{x}{M} - \frac{x_0}{M} \right)^{-n}. \quad (2)$$

Here, a is the decay coefficient, x is the downstream distance from the grid, x_0 is the virtual origin, and n is the power-law decay exponent. In this study, x_0 and n are estimated from the maximum decay range method²⁹ and the regression method,²⁸ where only the data in the far field ($x/M > 50$ for the double-random modes and $x/M > 40$ for the open mode) are used. The results of n are listed in Table II. So far, the values of n obtained in active-grid turbulence in previous studies fall in the range 1.2–1.4.¹¹ The relatively large variations of n in previous studies may be explained by a short streamwise distance covered in the experiments, where the data in the near field can be included in the estimation of n . In the present study, we extend the streamwise distance of the measurement to eliminate the influence of the near field on the estimation of n . Here, the values of n obtained for the double-random modes are close to 10/7 for Batchelor turbulence rather than

TABLE II. Turbulent Reynolds number and the decay exponent of u_{rms}^2 .

Case	Symbol	x/M	Re_λ	n
1	Diamond (dark yellow)	28–108	196–332	1.46 ± 0.02 ($x/M > 50$)
2	Circle (pink)	28–108	232–406	1.44 ± 0.03 ($x/M > 50$)
3	Up triangle (orange)	27–80	85–104	1.32 ± 0.03 ($x/M > 40$)

6/5 for Saffman turbulence. Note that different Re_σ leads to a similar value of n in the double-random mode in cases 1 and 2. Note also that Fig. 2 implies that the decay rate in the far field is larger than that in the near field: calculated n will be smaller if near-field data are included. The value of $n=1.32$ for the open mode is close to n obtained in passive-grid turbulence in previous studies at similar Re_M .^{6,11}

B. Integral length scale

Below this section, we will investigate the large-scale characteristics and the nondimensional dissipation rate $C_\epsilon (= \epsilon L / u_{rms}^3)$ for different modes of the active grid. We first examine the behavior of the integral length scale L . Figure 3 shows the variations of normalized integral length scale L/M with the streamwise distance. In the present study, L is calculated with two different methods: the first method is based on the integration of an autocorrelation function $f(r)$ of instantaneous streamwise velocity fluctuation $u(x)$ up to a first zero-crossing point, and the second method is based on the Rice theorem¹⁴ used by Mora and Obligado.³⁰ Taylor's hypothesis is used for both cases. The second method calculates L by $L = \pi \text{Var}(\Delta Z) / 4 \langle \Delta Z \rangle$, where ΔZ is the distance between zero-crossing points of the fluctuating velocity signal, $\langle \Delta Z \rangle$ is the average of ΔZ , and $\text{Var}(\Delta Z)$ is the variance of ΔZ . In this method, first, we apply the eighth-order Butterworth filter to acquire the fluctuating velocity signal at different frequencies and then calculate the signal zero-crossings and their number density n_s at each frequency. Mora and Obligado³⁰ stated that n_s is properly resolved if a plateau region appears for filter frequencies larger than a certain frequency. In the present study, we confirm that n_s shows a plateau region for a wide range of filter frequencies, and n_s is decided by the cutoff frequency. $\langle \Delta Z \rangle$ is then obtained by $\langle \Delta Z \rangle = 1/n_s$.¹⁴ The results show that L/M is larger for higher Re_σ , and so are the differences between the two calculation methods. Note that the first method leads to larger scatter and larger values of L compared with the second method. This is attributed to the fact that $f(r)$ often oscillates before its first zero-crossing or does not fall to zero. Therefore, we used the values of L calculated by the second method hereafter. It is shown that L/M slightly decreases with x/M for the double-random modes even in the far-downstream region. Similarly, Mora *et al.*¹³ showed that L slightly decreased with x/M in the near field. In the open mode, the

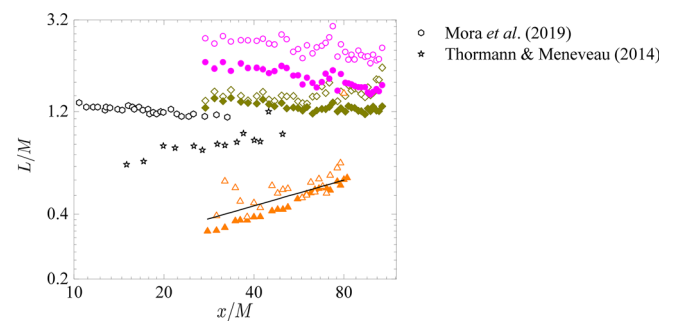


FIG. 3. Variations of normalized integral length scale with streamwise distance compared with previous studies. Open and closed symbols represent data obtained by $L = \int_0^\infty f(r) dr$ and $L = \pi \text{Var}(\Delta Z) / 4 \langle \Delta Z \rangle$, respectively. The solid line represents a power-law exponent of 2/5 for Saffman turbulence.⁴ For symbols in the present study, see Table II.

increasing of L/M with a streamwise distance in both calculation methods follows the similar trends in passive-grid turbulence in previous studies, where the exponent of the power law is close to $2/5$ for Saffman turbulence.^{4,5} It is noted, however, that the virtual origin is not considered in Fig. 3, and the comparison is only for reference. The magnitude of L/M for the open mode is smaller than those for the double-random modes. The comparison between the different modes of active grids proves that the motions of active grids influence the behavior of the integral length scale both in the near and far fields.

C. Properties of the energy cascade

1. Spectral characteristics

Figure 4 shows the normalized one-dimensional longitudinal energy spectra E_{11} for the double-random modes at $x/M = 30$ and 108. Data obtained from the open mode at $x/M = 80$ are also plotted. Here, Taylor's hypothesis is used to convert the frequency to longitudinal wavenumber k_1 . The dissipation rate ε is also calculated using Taylor's hypothesis with an assumption of isotropy by $\varepsilon = 15\nu(\frac{\partial u}{\partial x})^2$. The different spectra for the double-random mode are well collapsed beyond $k_1\eta \sim 0.02$. The Kolmogorov's $-5/3$ inertial subrange for the double-random modes is extended in comparison with the open mode due to larger Re_λ . In the dissipative range, the spectra for the double-random modes and the open mode are well collapsed beyond $k_1\eta \sim 0.1$, which has been confirmed in different types of flow.³¹

2. Structure functions

For HIT in the inertial subrange at sufficiently high Re_λ , the predictions with Kolmogorov hypotheses are embodied in

$$\overline{(\delta u(r))^2} = -\frac{4}{3}(\varepsilon r)^{2/3}, \quad (3)$$

$$\overline{(\delta u(r))^3} = -\frac{4}{5}\varepsilon r, \quad (4)$$

where $\delta u(r) = u(x+r) - u(x)$ is the streamwise velocity increment at the separation of two points r . Figure 5 provides the compensated second-order structure functions for the double-random and open modes with different Re_λ and streamwise distance. Generally, the plateau regions for the double-random modes can be seen clearly in the range $20 < r/\eta < 200$, while the plateau region is hardly seen for the

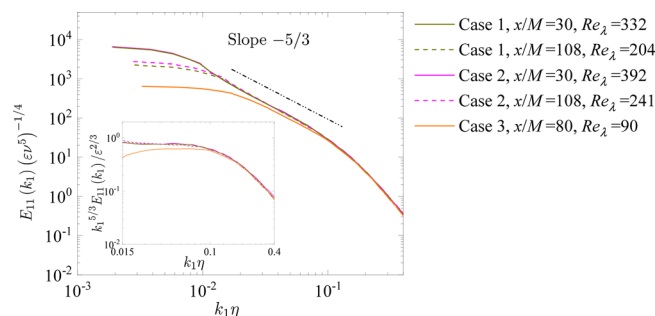


FIG. 4. Normalized one-dimensional longitudinal energy spectra and compensated spectra (inset).

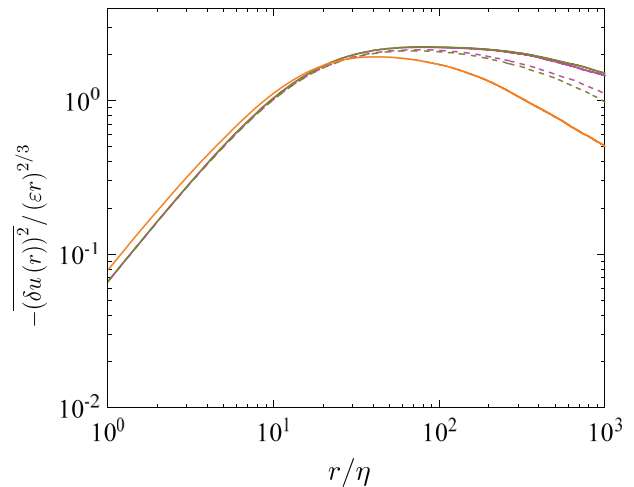


FIG. 5. Distributions of $-(\delta u(r))^2 / (\varepsilon r)^{2/3}$ vs r/η . Lines are the same as in Fig. 4.

open mode. This suggests that the Kolmogorov hypotheses are only established at high Re_λ , as expected.

The compensated third-order structure functions are shown together with previous studies in Fig. 6. It can be seen that the compensated third-order structure functions for the double-random mode in the near field ($x/M = 30$) are larger than the theoretical value of $4/5$ for HIT, which was also observed in previous studies of circular jet.³² The shear stress arising from inhomogeneity in the near field could be a reason for the large value. In contrast, the compensated third-order structure functions for the double-random modes in the far field ($x/M = 80$) are close to $4/5$, suggesting that the high- Re_λ is the premise of Kolmogorov hypotheses.³² However, the present compensated third-order structure functions for the double-random mode in the far field are slightly smaller than $4/5$, and this tendency is also consistent with previous observations of active-grid turbulence in Mydlarski and Warhaft.⁹

3. Dissipation characteristics

Hereafter, only the data in the far field of $x/M > 40$ are plotted for the open mode to eliminate the near-field effects, while all data are plotted for the double-random modes. Figure 7 shows the dependence of $C_\varepsilon = \varepsilon L / u_{rms}^3$ on Re_λ , compared with previous studies on passive-grid turbulence⁶ and active-grid turbulence.^{13,20,21} Previous numerical and experimental studies show that C_ε is close to one for decaying HIT,^{33–35} while $C_\varepsilon \approx 0.5$ is established for forced stationary HIT.^{3,36} In the present study, C_ε for the open mode is close to those obtained in passive-grid turbulence in previous studies.⁶ However, for the double-random modes, C_ε is around 0.5 and smaller than one.^{13,20} Furthermore, this asymptotic value is different from those reported in previous active-grid turbulence experiments.^{13,20,21} To investigate this, we will revisit the analysis of Mazellier and Vassilicos.¹⁴

According to Mazellier and Vassilicos,¹⁴ using the definitions of η and C_ε with $\varepsilon = 15\nu u_{rms}^2 / \lambda^2$, C_ε can be expressed as

$$C_\varepsilon = K(C^3/A^2)C_s^3, \quad (5)$$

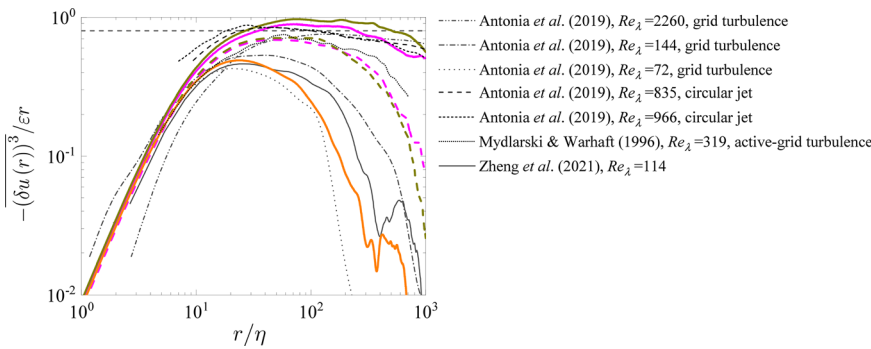


FIG. 6. Distributions of $-(\delta u(r))^3 / \epsilon r$ vs r/η . Lines of the present study (color lines) are the same as in Fig. 4.

where $K = (15\pi^2)^{3/2}$ is a constant, C is the intermittency constant that reflects the non-Gaussianity of velocity derivatives $\partial u / \partial x$, $A = \eta^* / \eta$ is the normalized inner cutoff scale η^* below which new stagnation points of u do not exist, and C'_s is the dimensionless number characterizing the largest eddies of turbulence. Here, A is also called “the range of viscous scales of the turbulence.” The calculation of C'_s is given by

$$C'_s = n_s^* L (L/\eta^*)^{-2/3}, \quad (6)$$

where n_s^* is the number density n_s at the inner cutoff frequency. Following the Rice theorem,¹⁴ $n_s^{-1} = C\pi\lambda$ is applied. In the present study, calculations of η^* use the same process mentioned by Mazellier and Vassilicos.¹⁴ Equation (5) is examined by plotting $K(C^3/A^2)C'_s$ against C_e in Fig. 8. It can be seen that Eq. (5) reasonably holds in active-grid turbulence as well as in other types of flows complied by Mazellier and Vassilicos.¹⁴ This result supports the correction due to non-Gaussian effect, C , and the assertion that Eq. (5) is universal.¹⁴ The Re_λ dependencies of A , C^3 , C^3/A^2 , and C'_s are discussed below. The data include turbulence generated by an active grid in Mora *et al.*¹³ and different flows (turbulence generated by regular and fractal grids, jet,

and wind tunnel data of ONERA at Modane) compiled in Mazellier and Vassilicos.¹⁴ Figure 9(a) shows Re_λ dependence of A . The data in active-grid turbulence (i.e., present data and Mora *et al.*¹³) tend to be smaller than those in other types of flows.¹⁴ The result suggests that the range of viscous scales is smaller in active-grid turbulence. Figure 9(b) shows Re_λ dependence of C^3 . The non-Gaussian effect (or intermittency) tends to be significant in active-grid turbulence as attested by larger C^3 for the active grid than for the open mode (passive grid). For higher Re_λ , especially for $Re_\lambda > 10^3$, more experimental data are required to investigate the Re_λ dependence of C^3 . Figure 9(c) shows Re_λ dependence of C^3/A^2 . The values of C^3/A^2 in active-grid turbulence is larger than the broken line obtained in previous studies because of the smaller range of viscous scales and stronger intermittency, namely, smaller A and larger C . Figure 9(d) shows Re_λ dependence of C'_s . As confirmed in Mazellier and Vassilicos,¹⁴ C'_s depends on a type of flow, while its dependence on Re_λ is weak when one compares C'_s among all the flows shown in the figure. From above, C_e of the active-grid turbulence is different from that for the open mode (or in passive-grid turbulence) due to the different large- and small-scale characteristics, which are manifested as different values of C'_s and C^3/A^2 , respectively.

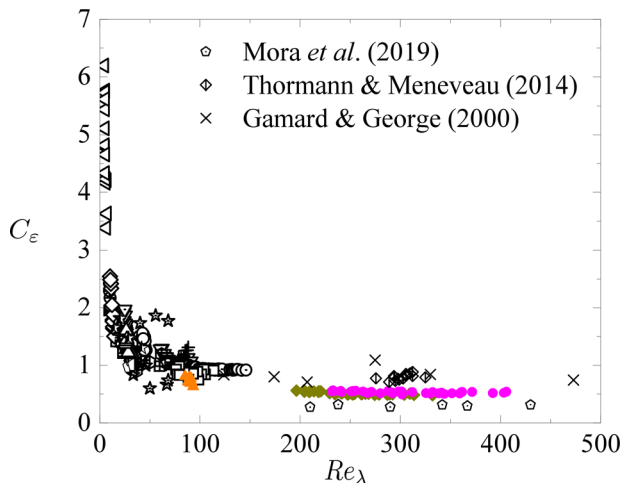


FIG. 7. Dependence of C_e on Re_λ together with previous studies on passive-grid turbulence, see Zheng *et al.* and references therein.⁶ Data of active-grid turbulence^{13,20,21} are also plotted. For symbols in the present study (color plots), see Table II.

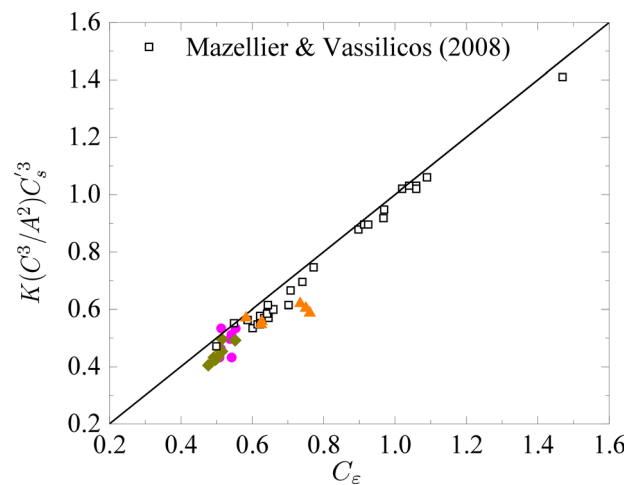


FIG. 8. Plots of $K(C^3/A^2)C'_s$ vs C_e . For symbols in the present study (color plots), see Table II.

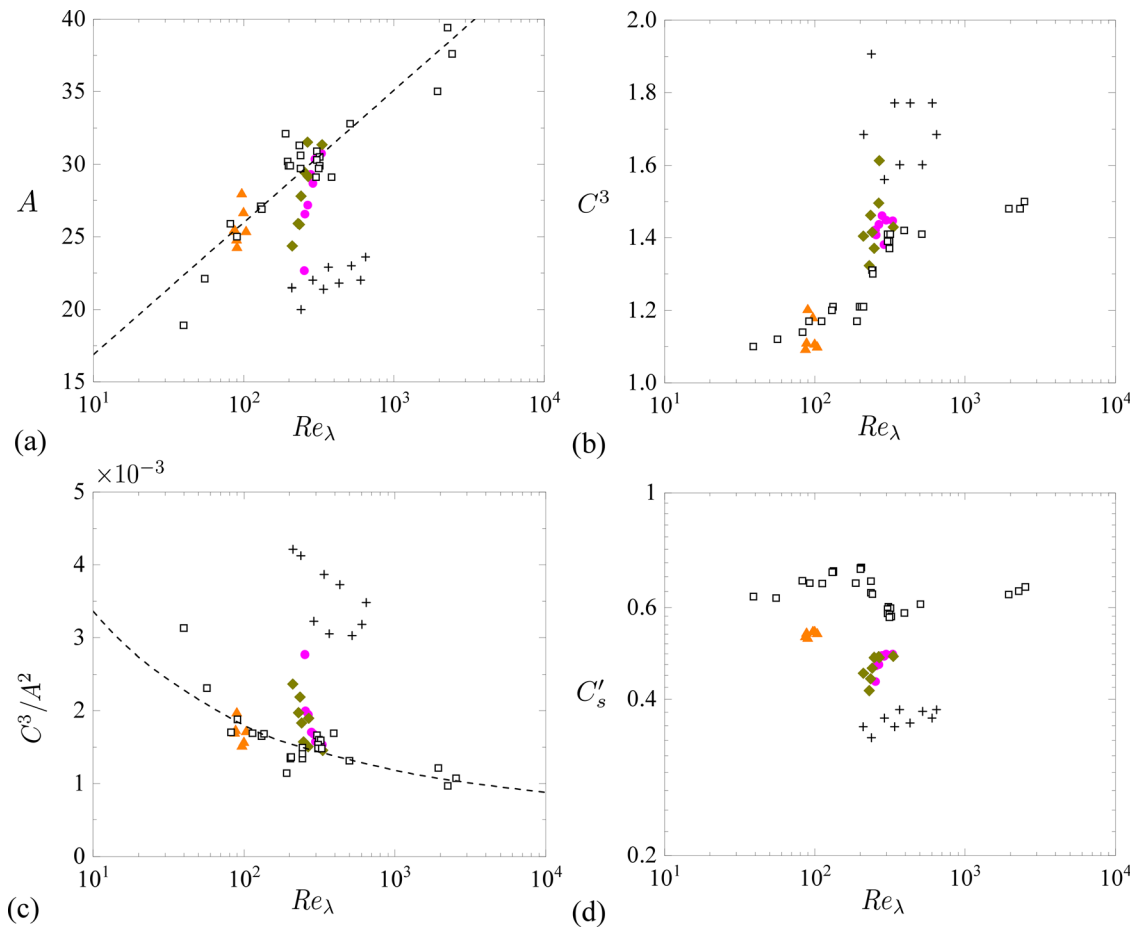


FIG. 9. Re_λ variations of (a) A , (b) C^3 , (c) C^3/A^2 , and (d) C'_s . The dashed lines in (a) and (c) are $A = 7.8 + 9.1 \log Re_\lambda$ and $C^3/A^2 = (0.87 + 0.11 \log Re_\lambda)^2 / (7.8 + 9.1 \log Re_\lambda)^2$, respectively, obtained by fitting the experimental data in Mazellier and Vassilicos.¹⁴ The open-square symbols denote the data in different flows compiled in Mazellier and Vassilicos,¹⁴ and the cross symbols are obtained in the active-grid turbulence by Mora *et al.*¹³ For symbols in the present study (color plots), see Table II.

Figure 10 shows the evolutions of L/λ . In an equilibrium HIT, $L/\lambda = C_e Re_\lambda / 15$ holds with a constant C_e .^{13,16} The solid and dashed lines use $C_e = 0.74$ and 0.53 in $L/\lambda = C_e Re_\lambda / 15$, respectively. In the present study, $L/\lambda = C_e Re_\lambda / 15$ is well sustained for different modes of the active grid. Although the integral length scales for the double-random modes decrease slightly with the streamwise distance and Re_λ , the equilibrium scaling of the energy cascade is still established for the double-random modes. As a result, motions of active grids do not break the classical energy cascade in the far field. In the open mode, L/λ remains almost constant since the range of Re_λ is small. Thus, it is difficult to assess whether or not the turbulence is in an equilibrium state.

To highlight some hints and further elucidate the equilibrium scaling of active-grid turbulence, we note previous studies using passive grids. Hurst and Vassilicos³⁷ found that the integral length scale of turbulence generated by the space-filling fractal grids remains approximately constant along streamwise direction. Seoud and Vassilicos³⁸ further stated that L/λ is constant regardless of Re_λ , and C_e behaved as a function of Re_λ , i.e., $C_e \sim Re_\lambda^{-1}$. Note that these

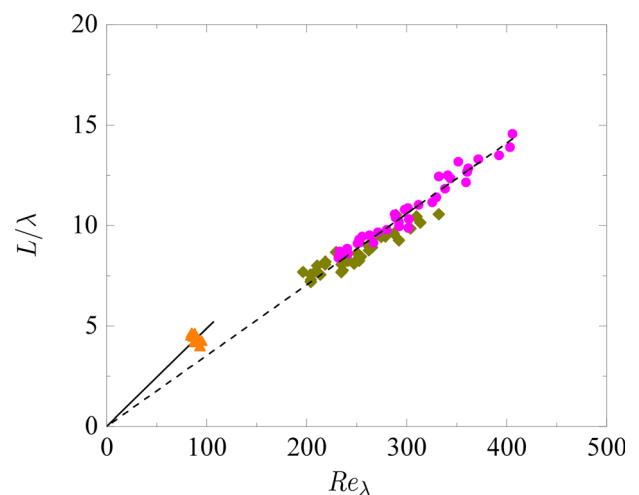


FIG. 10. Relationship between L/λ and Re_λ . For symbols, see Table II.

observations are made in the near field. Valente and Vassilicos¹⁷ further confirmed that in the near field, both the conventional (regular) and fractal grids follow the nonequilibrium scaling $C_e = f(Re_M)/Re_\lambda$. Nagata *et al.*³⁹ also confirmed this relation for some specific geometry of grids. Furthermore, Hearst and Lavoie¹⁹ confirmed similar nonequilibrium observations in the near field of the fractal-grid turbulence, but proved that $L/\lambda \propto C_e Re_\lambda$ with a constant C_e is established in the far field. In conclusion, combined with the previous observations of passive- (both conventional and fractal) and active-grid turbulence, the equilibrium energy cascade in the far field is approximately established in grid turbulence despite the different turbulence-generating conditions with grids.

D. Variations of quantities related to enstrophy

The Re_λ variations of velocity derivative skewness S [Eq. (1)] and flatness F ,

$$F = \frac{\overline{\left(\frac{\partial u}{\partial x}\right)^4}}{\left[\overline{\left(\frac{\partial u}{\partial x}\right)^2}\right]^2}, \quad (7)$$

are investigated to see the small-scale characteristics. Here, Taylor's hypothesis is used to convert the time derivative to spatial one. In Figs. 11(a) and 11(b), both $-S$ and F agree well with previous studies in different flows, and both of them slightly increase with Re_λ .⁶ The ratio $-S/F^{3/8}$ is also plotted in Fig. 11(c), including shear-flow data taken from Champagne⁴⁰ and active-grid turbulence data from Mydlarski and Warhaft.⁹ The results of $-S/F^{3/8}$ range 0.2–0.25 regardless of Re_λ , and in accordance with the prediction of Wyngaard and Tennekes⁴¹ that $-S \propto F^{3/8}$. These results indicate that the small-scale characteristics in the far field of active-grid turbulence are consistent with those in previous studies.

The rates of production and destruction of enstrophy in HIT are, respectively, represented by $-S$ and $2G/Re_\lambda$. Figure 12 shows the variations of $S + 2G/Re_\lambda$. Zheng *et al.*⁶ elucidated that although the

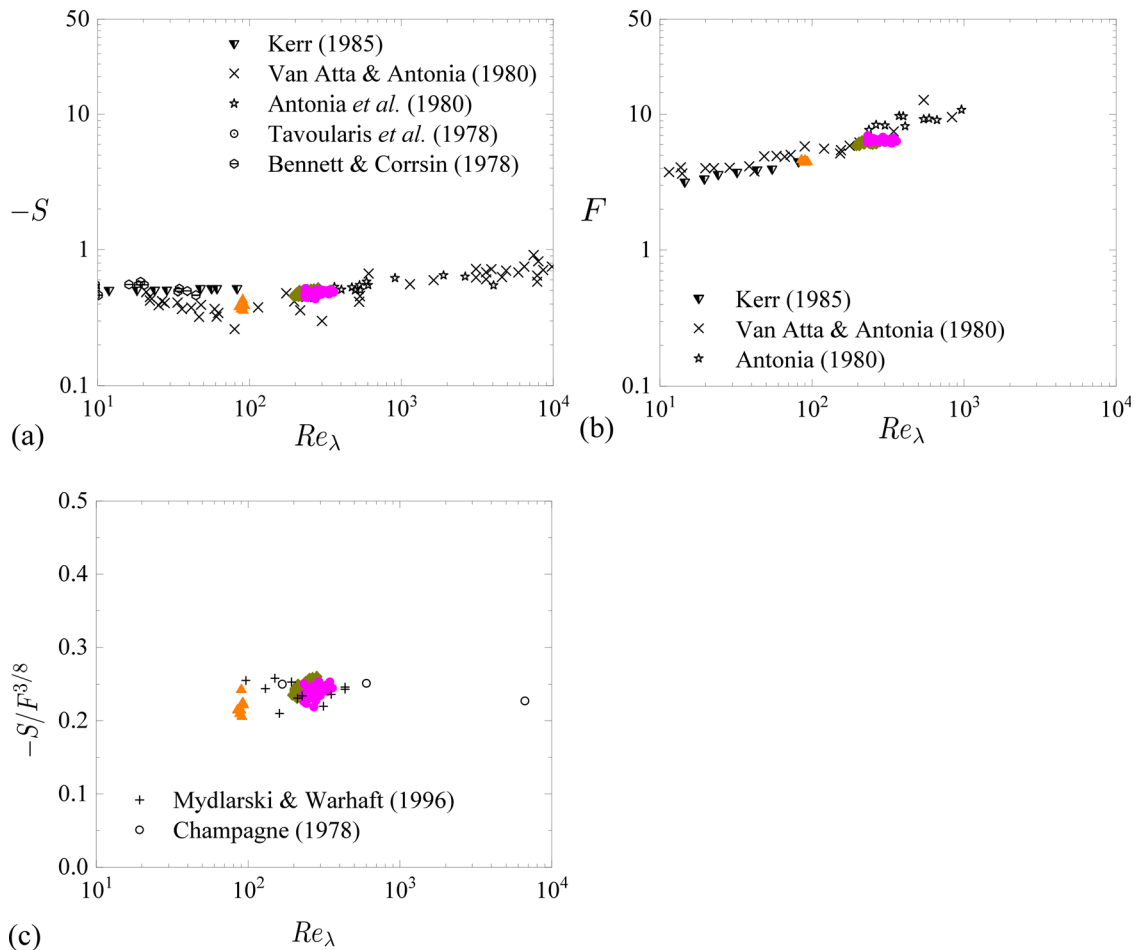


FIG. 11. Re_λ variations of (a) the velocity derivative skewness $-S$, (b) the velocity derivative flatness F , and (c) $-S/F^{3/8}$ together with the data in Mydlarski and Warhaft⁹ and Champagne.⁴⁰ In (a) and (b), the data on the passive grid and other compiled data⁶ are also plotted. See Zheng *et al.*⁶ and references therein. For symbols in the present study (color plots), see Table II.

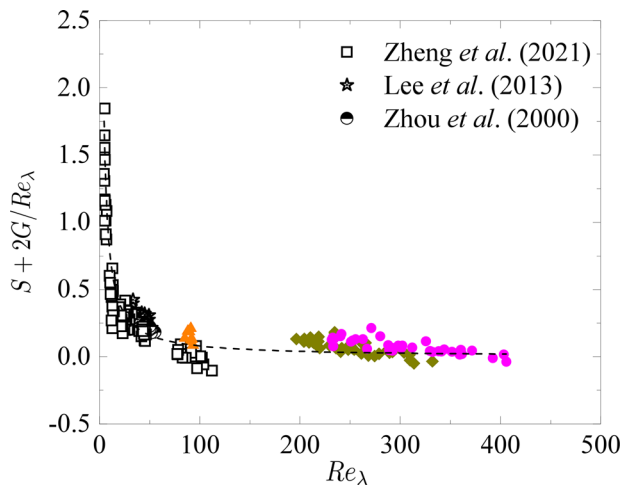


FIG. 12. Variations of $S + 2G/Re_\lambda$ with Re_λ together with previous studies, see Zheng *et al.* and references therein.⁶ Dashed line represents a power-law exponent of -1 . For symbols in the present study (color plots), see Table II.

imbalance between production and destruction of enstrophy is significant at very low Re_λ , it becomes negligible as Re_λ increases. In the present study, we further give experimental evidence that the production and destruction are roughly balanced with each other from moderate to high Re_λ in active-grid turbulence. Furthermore, the present data in both the passive- and active-grid turbulences are consistent with the relation $S + 2G/Re_\lambda \sim Re_\lambda^{-1}$. This finding supports that the motions of active grid are not significant to the enstrophy budget, compared with the influence of Re_λ .

Finally, we note the connections between the equilibrium behavior and the production and destruction of enstrophy for the active-grid turbulence. First, for the near field of the fractal-grid turbulence, Seoud and Vassilicos³⁸ attributed the nonequilibrium behaviors to “either the combined vortex stretching and strain rate production processes are inhibited, or no more strain rate fluctuations with increasing Re_λ .” Later, Hearst and Lavoie⁴² inferred that the nonequilibrium region is related to the residual strain produced from the turbulence generating conditions of the fractal grid. They showed that while the strain becomes nearly constant, the fractal-grid turbulence reaches an equilibrium state.⁴² This leads to the possibility that the nonequilibrium behavior is dependent on the combined vortex stretching and strain rate production processes. In the present study, variations of $-S$ for the double-random modes with Re_λ are small in the far field of active-grid turbulence. Moreover, the balance between the production and destruction of enstrophy indicates that the equilibrium behavior in the far field of active-grid turbulence is reasonable compared with the near field of passive grids.

IV. CONCLUSIONS

Turbulent characteristics, energy transfer, and the enstrophy production and destruction have been investigated in the far field of active-grid turbulence at $Re_M = 33\,000$. The double-random mode with different Rossby numbers $R_o = 40$ (case 1) and 80 (case 2) and the open mode are employed. In the present study, the velocity

measurements using hot-wire anemometry are conducted at up to $x/M = 108$. The main results are summarized as follows.

For the energy decay of active-grid turbulence, the power-law decay exponents $n = 1.46$ for case 1 and $n = 1.44$ for case 2 are obtained. These values of n are consistent with Makita,⁸ suggesting that the influence of R_o is negligible for the energy decay in the far field of active-grid turbulence. For the open mode, the value of n is consistent with the results of previous passive-grid turbulence.⁶

The behavior of the integral length scale L is examined in the far field of active-grid turbulence, which has not been reported in previous studies. Mora *et al.*¹³ observed the decreasing trend of L with the streamwise distance in the near field. It is identified that L for the double-random modes slightly decreases in the far field, while for the open mode, it increases with the streamwise distance as obtained in the passive-grid turbulence. The present experimental evidence of L suggests that the motions of the active grid influence the behavior of L even in the far field.

The third-order structure functions obtained in the far field are close to that obtained by the active grid in Mydlarski and Warhaft,⁹ while those obtained in the near field are close to the data in the circular jet,³² indicating the possibility of the influence of inhomogeneity in the near field. Furthermore, the compensated second- and third-order structure functions suggest that the Kolmogorov hypotheses are only established in high turbulent Reynolds numbers, as already suggested.³²

For the dissipation characteristics, C_ϵ for the double-random modes is around 0.5 and smaller than one. This asymptotic value is different from those reported in previous active-grid turbulence experiments and could be nonuniversal.¹⁴ We revisited the analysis of Mazellier and Vassilicos¹⁴ and found that the present active-grid turbulence has a smaller number of large-scale eddies, smaller range of viscous scales, and stronger small-scale intermittency, which lead to a different value of C_ϵ . Although L decreases with the streamwise distance, the establishment of $L/\lambda = C_\epsilon Re_\lambda / 15$ with a constant C_ϵ indicates that the far field active-grid turbulence satisfies the equilibrium scaling, which has been confirmed in the far field of passive-grid turbulence. Thus, it is found that the grid motions do not influence the behavior of the equilibrium energy cascade in the far field.

The Re_λ dependences of the velocity derivative skewness $-S$ and the velocity derivative flatness F show good agreement with previous studies and both of them slightly increase with Re_λ . The relation $-S \propto F^{3/8}$ is also confirmed in the present active-grid turbulence, and the magnitude of $-S/F^{3/8}$ is consistent with previous studies.^{9,40} $S + 2G/Re_\lambda \sim Re_\lambda^{-1}$ is established in the active-grid turbulence, regardless of the active-grid motions. The equilibrium state of the active-grid turbulence is somehow related to the balance of the production and destruction of the enstrophy.

ACKNOWLEDGMENTS

The authors would like to thank Mr. Tetsuya Matsushima (Nagoya University) and Mr. Jinyu Li (Nagoya University) for their cooperation in conducting the experiments. They also thank Dr. Yasuo Hattori in Central Research Institute of Electric Power Industry for his help in constructing the active grid and Professor Susumu Goto (Osaka University) for his valuable comments to this study. This study was supported by the JSPS KAKENHI, Grant No.

18H01367. The first author was financially supported by the DII collaborative Graduate Program for Accelerating Innovation in Future Electronics, Nagoya University.

AUTHOR DECLARATIONS

Conflict of Interest

The authors have no conflicts to disclose.

DATA AVAILABILITY

The data that support the findings of this study are available from the corresponding author upon reasonable request.

REFERENCES

- ¹G. I. Taylor, "Production and dissipation of vorticity in a turbulent fluid," *Proc. R. Soc. A* **164**, 15–23 (1938).
- ²A. N. Kolmogorov, "On the degeneration of isotropic turbulence in an incompressible viscous fluid," *Dokl. Akad. Nauk SSSR* **31**, 538–541 (1941).
- ³W. J. T. Bos, L. Shao, and J.-P. Bertoglio, "Spectral imbalance and the normalized dissipation rate of turbulence," *Phys. Fluids* **19**, 045101 (2007).
- ⁴T. Kitamura, K. Nagata, Y. Sakai, A. Sasoh, O. Terashima, H. Saito, and T. Harasaki, "On invariants in grid turbulence at moderate Reynolds numbers," *J. Fluid Mech.* **738**, 378–406 (2014).
- ⁵T. Watanabe and K. Nagata, "Integral invariants and decay of temporally developing grid turbulence," *Phys. Fluids* **30**, 105111 (2018).
- ⁶Y. Zheng, K. Nagata, and T. Watanabe, "Energy dissipation and enstrophy production/destruction at very low Reynolds numbers in the final stage of the transition period of decay in grid turbulence," *Phys. Fluids* **33**, 035147 (2021).
- ⁷A. N. Kolmogorov, "Dissipation of energy in the locally isotropic turbulence," *Dokl. Akad. Nauk SSSR* **32**, 16 (1941); English translation by V. Levin, *Proc. R. Soc. Lond. A* (1991) **434**, 15–17; available at <http://www.jstor.org/stable/51981>.
- ⁸H. Makita, "Realization of a large-scale turbulence field in a small wind tunnel," *Fluid Dyn. Res.* **8**, 53–64 (1991).
- ⁹L. Mydlarski and Z. Warhaft, "On the onset of high-Reynolds-number grid-generated wind tunnel turbulence," *J. Fluid Mech.* **320**, 331–368 (1996).
- ¹⁰J. V. Larssen and W. J. Devenport, "On the generation of large-scale homogeneous turbulence," *Exp. Fluids* **50**, 1207–1223 (2011).
- ¹¹C. S. Shet, M. R. Cholevari, and S. V. Veeravalli, "Optimizing the performance of an active grid to generate high intensity isotropic free stream turbulence," *Phys. Fluids* **32**, 095120 (2020).
- ¹²A. Azzam and P. Lavoie, "Experimental investigation of unsteady turbulence using an active grid," in *Proceedings of 11th International Symposium on Turbulence and Shear Flow Phenomena* (2019).
- ¹³D. O. Mora, E. M. Pladellorens, P. R. Turró, M. Lagauzere, and M. Obligado, "Energy cascades in active-grid-generated turbulent flows," *Phys. Rev. Fluids* **4**, 104601 (2019).
- ¹⁴N. Mazellier and J. Vassilicos, "The turbulence dissipation constant is not universal because of its universal dependence on large-scale flow topology," *Phys. Fluids* **20**, 015101 (2008).
- ¹⁵R. J. Hearst and P. Lavoie, "The effect of active grid initial conditions on high Reynolds number turbulence," *Exp. Fluids* **56**, 185 (2015).
- ¹⁶P. C. Valente and J. C. Vassilicos, "The decay of turbulence generated by a class of multiscale grids," *J. Fluid Mech.* **687**, 300–340 (2011).
- ¹⁷P. C. Valente and J. C. Vassilicos, "Universal dissipation scaling for nonequilibrium turbulence," *Phys. Rev. Lett.* **108**, 214503 (2012).
- ¹⁸J. C. Isaza, R. Salazar, and Z. Warhaft, "On grid-generated turbulence in the near-and far field regions," *J. Fluid Mech.* **753**, 402–426 (2014).
- ¹⁹R. J. Hearst and P. Lavoie, "Decay of turbulence generated by a square-fractal-element grid," *J. Fluid Mech.* **741**, 567–584 (2014).
- ²⁰A. Thormann and C. Meneveau, "Decay of homogeneous, nearly isotropic turbulence behind active fractal grids," *Phys. Fluids* **26**, 025112 (2014).
- ²¹S. Gamard and W. K. George, "Reynolds number dependence of energy spectra in the overlap region of isotropic turbulence," *Flow, Turbul. Combust.* **63**, 443–477 (2000).
- ²²T. Zhou, R. A. Antonia, L. Danaïla, and F. Anselmetti, "Transport equations for the mean energy and temperature dissipation rates in grid turbulence," *Exp. Fluids* **28**, 143–151 (2000).
- ²³S. K. Lee, L. Djenidi, R. A. Antonia, and L. Danaïla, "On the destruction coefficients for slightly heated decaying grid turbulence," *Int. J. Heat Fluid Flow* **43**, 129–136 (2013).
- ²⁴F. Thiesset, R. A. Antonia, and L. Danaïla, "Consequences of self-preservation on the axis of a turbulent round jet," *J. Fluid Mech.* **748**, R2 (2014).
- ²⁵G. K. Batchelor and A. A. Townsend, "Decay of vorticity in isotropic turbulence," *Proc. R. Soc. A* **190**, 534–550 (1947).
- ²⁶L. Mydlarski, "A turbulent quarter century of active grids: From Makita (1991) to the present," *Fluid Dyn. Res.* **49**, 061401 (2017).
- ²⁷J. Mi, R. C. Deo, and G. J. Nathan, "Fast-convergent iterative scheme for filtering velocity signals and finding Kolmogorov scales," *Phys. Rev. E* **71**, 066304 (2005).
- ²⁸M. S. Mohamed and J. C. LaRue, "The decay power law in grid-generated turbulence," *J. Fluid Mech.* **219**, 195–214 (1990).
- ²⁹P. Lavoie, L. Djenidi, and R. A. Antonia, "Effects of initial conditions in decaying turbulence generated by passive grids," *J. Fluid Mech.* **585**, 395–420 (2007).
- ³⁰D. O. Mora and M. Obligado, "Estimating the integral length scale on turbulent flows from the zero crossings of the longitudinal velocity fluctuation," *Exp. Fluids* **61**, 199 (2020).
- ³¹S. B. Pope, *Turbulent Flows* (IOP Publishing, 2001).
- ³²R. A. Antonia, S. L. Tang, L. Djenidi, and Y. Zhou, "Finite Reynolds number effect and the 4/5 law," *Phys. Rev. Fluids* **4**, 084602 (2019).
- ³³P. Burattini, P. Lavoie, and R. A. Antonia, "On the normalized turbulent energy dissipation rate," *Phys. Fluids* **17**, 098103 (2005).
- ³⁴K. R. Sreenivasan, "On the scaling of the turbulence energy dissipation rate," *Phys. Fluids* **27**, 1048–1051 (1984).
- ³⁵J. C. Vassilicos, "Dissipation in turbulent flows," *Annu. Rev. Fluid Mech.* **47**, 95–114 (2015).
- ³⁶L. P. Wang, S. Chen, J. G. Brasseur, and J. C. Wyngaard, "Examination of hypotheses in the Kolmogorov refined turbulence theory through high-resolution simulations. Part 1. Velocity field," *J. Fluid Mech.* **309**, 113–156 (1996).
- ³⁷D. Hurst and J. C. Vassilicos, "Scalings and decay of fractal-generated turbulence," *Phys. Fluids* **19**, 035103 (2007).
- ³⁸R. E. Seoud and J. C. Vassilicos, "Dissipation and decay of fractal-generated turbulence," *Phys. Fluids* **19**, 105108 (2007).
- ³⁹K. Nagata, T. Saiki, Y. Sakai, Y. Ito, and K. Iwano, "Effects of grid geometry on non-equilibrium dissipation in grid turbulence," *Phys. Fluids* **29**, 015102 (2017).
- ⁴⁰F. H. Champagne, "The fine-scale structure of the turbulent velocity field," *J. Fluid Mech.* **86**, 67–108 (1978).
- ⁴¹J. C. Wyngaard and H. Tennekes, "Measurements of the small-scale structure of turbulence at moderate Reynolds numbers," *Phys. Fluids* **13**, 1962–1969 (1970).
- ⁴²R. J. Hearst and P. Lavoie, "Velocity derivative skewness in fractal-generated, non-equilibrium grid turbulence," *Phys. Fluids* **27**, 071701 (2015).